J. Fluid Mech. (2005), *vol.* 544, *pp.* 143–171. © 2005 Cambridge University Press
doi:10.1017/S0022112005006567 Printed in the United Kingdom

Experimental study of a turbulent buoyant helium plume

By T. J. O'HERN[1], E. J. WECKMAN[2], A. L. GERHART[3], S. R. TIESZEN[1] AND R. W. SCHEFER[4]

[1]Engineering Sciences Center, Sandia National Laboratories, Albuquerque, NM 87185, USA
[2]Mechanical Engineering Department, University of Waterloo, Waterloo, Ontario, N2L 3G1, Canada
[3] Mechanical Engineering Department, Lawrence Technological University, Southfield, MI 48075-1058, USA
[4]Diagnostic and Reacting Flow Department, Sandia National Laboratories, Livermore, CA 94551, USA

(Received 2 December 2004 and in revised form 6 July 2005)

An experimental study has been performed on the dynamics of a large turbulent buoyant helium plume. Two-dimensional velocity fields were measured using particle image velocimetry (PIV) while helium mass fraction was determined by planar laser-induced fluorescence (PLIF). PIV and PLIF were performed simultaneously in order to obtain velocity and mass fraction data over a plane that encompassed the plume core, the near-field mixing zones and the surrounding air. The Rayleigh–Taylor instability at the base of the plume leads to the vortex that grows to dominate the flow. This process repeats in a cyclical manner. The temporally and spatially resolved data show a strong negative correlation between density and vertical velocity, as well as a strong 90° phase lag between peaks in the vertical and horizontal velocities throughout the flow field owing to large coherent structures associated with puffing of the turbulent plume. The joint velocity and mass fraction data are used to calculate Favre-averaged statistics in addition to Reynolds-(time) averaged statistics. Unexpectedly, the difference between both the Favre-averaged and Reynolds-averaged velocities and second-order turbulent statistics is less than the uncertainty in the data throughout the flow field. A simple analysis was performed to determine the expected differences between Favre and Reynolds statistics for flows with periodic fluctuations in which the density and velocity fields are perfectly correlated, but have the phase relations as suggested by the data. The analytical results agree with the data, showing that the Favre and Reynolds statistics will be the same to lead order. The combination of observation and simple analysis suggests that for buoyancy-dominated flows in which it can be expected that density and velocity are strongly correlated, phase relations will result in only second-order differences between Favre- and Reynolds-averaged data in spite of strong fluctuations in both density and velocity.

1. Introduction

Buoyant plumes are encountered in many flows of engineering and environmental importance, including fires, subsea and atmospheric exhaust phenomena, gas releases and geothermal events. Previous studies of buoyant helium plumes (e.g. Cetegen & Kasper 1996; Shabbir & George 1994) were performed at relatively small scale. Many other studies have examined momentum-dominated buoyant jets (e.g. Papanicolaou & List 1988) where buoyancy effects only become dominant far downstream of the source. The goal of this work is to extend existing studies of the behaviour of

buoyancy-dominated plumes to near-source regions through measurements of velocity and mass fraction in large fully turbulent plumes. This paper describes a diagnostic technique for acquisition of temporally- and spatially-resolved data in buoyant turbulent fluid flows and presents and discusses the data acquired in a large helium plume. This work is motivated by the need to develop and validate numerical simulation tools for such flows. New numerical techniques, such as large eddy simulation (LES), have combined spatial and temporal resolution that cannot be fully validated by traditional point-measurement techniques, from which data are not spatially correlated. Unlike momentum-driven flows in which scalar fields, such as species, tend to be uncoupled from the flow (i.e. passive), in buoyant flows the scalar field gradients are coupled directly to the momentum field through the presence of the density–gravity product in the momentum source term. In particular, the density field is required in order to determine buoyancy effects in a buoyant turbulent plume. Therefore, it is necessary to have simultaneous measurements of both the density and the velocity fields. The combined temporally- and spatially-resolved velocity and density data are then used to determine such parameters as the Favre-averaged velocity statistics. The approach taken here is to apply simultaneously two planar imaging techniques: particle image velocimetry (PIV) for velocity field measurements and planar laser-induced fluorescence (PLIF) for scalar field measurements (mass fraction). These non-invasive optical techniques have been developed and applied in laboratory flows for years; however, they have not often been employed at a scale sufficient to be of use for developing validation data in fully turbulent buoyancy-dominated flows. While previous studies have made measurements of velocity using PIV (Cetegen 1997) and of time-resolved mass fraction in helium plumes and jets (Pasumarthi & Agrawal 2003), the scale of the present work and the simultaneous acquisition of velocity and mass fraction are unique. Measurements were made with sufficient spatial and temporal resolution to provide unique insights into the structure of the plume near the inlet. Two modes of turbulence are important, the large-scale puffing often seen in buoyant plumes and classical Rayleigh–Taylor instability causing air spikes and helium bubbles at the plume base.

The goals of this work are to examine the characteristics of turbulent buoyant plumes through combined velocity and concentration measurements and to use the data for the development and validation of subgrid scale turbulence models (DesJardin *et al.* 2000, 2004). These models will be incorporated into a fire simulation code currently under development. The helium plume experiments are an important step in developing the fire model, since the generation of turbulence due to buoyancy can be studied, uncoupled from the complexities of combustion chemistry. The region of interest in this study is the near-source region of the plume where the velocity is minimized. In this region, the ratio of buoyant forcing to advection is maximized resulting in the strongest buoyant effects on the flow field. The buoyant acceleration creates a region of strong entrainment and mixing and, for fires, combustion intensity, creating the greatest fire safety risk in reacting fire plumes. This emphasis is quite different from those studies that have examined the self-similar far-field of buoyant plumes (e.g. Dai & Faeth 1996). This paper presents and discusses only helium plume results; for methane and hydrogen fire data acquired using similar techniques see Tieszen *et al.* (2002, 2004*a*).

2. Experimental set-up

The experiment was designed to be a clean canonical buoyant plume so that the results would be of use beyond the specific geometry used here. Buoyant flows require

a minimum scale to become fully turbulent that is typically much larger than for momentum-driven flows. Unlike momentum-driven flows where vorticity is generated along the flow boundaries, turbulence in buoyant flows is primarily generated within the interior of the flow through a baroclinic mechanism. Unlike momentum-driven flows in which the distance to transition to turbulence can be shortened by increasing the inlet velocity at a fixed scale, in buoyant flows the baroclinic vorticity generation cannot be arbitrarily increased since it is determined by the pressure gradient and density gradient in the flow. The only way to reduce the distance to transition in a buoyant flow is to increase its scale. The 1 m source diameter of the present experiment was chosen as the smallest that would ensure that the plume would be fully turbulent, based on the flow characteristics of pool fires (another type of buoyant plume) through the fuel regression data of Blinov & Khudyakov (1961). The large scale of this experiment is therefore determined by the need to achieve a fully turbulent high-Richardson-number buoyant plume. Once the 1 m scale was chosen, the experiment had to be designed accordingly. An unconfined plume was not a reasonable option, since the flow would then be dominated by uncontrollable winds. The details of the enclosure are given below.

2.1. *FLAME facility and buoyant plume flow apparatus*

Experiments were performed in a large building designed for indoor fire experiments: the Fire Laboratory for Accreditation of Models by Experimentation (FLAME). This facility is shown schematically in figure 1. The central FLAME chamber is nominally a 6.1 m cubical enclosure. The ceiling converges to the outlet, a square chimney that is nominally 2.4 m on each side. The plume source is centred in the main chamber, elevated 2.45 m off the floor. The bottom and four sides of the facility are enclosed except for four inlet air ducts. Air is forced into FLAME through ducts situated at the four corners near its base using four independent variable flow rate fans, each with a maximum output of 4.7 standard $m^3 s^{-1}$. The inlet air is directed through a series of diverters, screens and honeycombs to form an annular low-velocity inlet flow surrounding the helium plume (figure 1). The facility layout and experiment were designed using numerical simulations such that the flow configuration within the enclosure models an unconfined plume on an infinite ground plane, i.e. external wind effects are minimized (Tieszen *et al.* 1998). Complete characterization of the uniformity of flow through the air inlets has been made, showing that the supply air is uniform to within 10 % around the annular inlet to FLAME (Blanchat 2001).

The plume source is 1 m in diameter and is surrounded by a 0.51 m wide sheet steel floor, which simulates a 'ground plane' by causing air being entrained by the accelerating plume to flow radially inward over the steel floor. Helium at 1.36 MPa is supplied from a bottle farm and enters the base of a 3 m tall diffuser through a 5.1 cm diameter tube in the centre of, and aligned coaxially with, a 1 m diffuser. The pressure in the diffuser is nearly ambient. As a consequence, the flow is choked at the exit of the discharge tube. The resulting jet flow into the diffuser is broadened by a series of three perforated plates with decreasing hole diameters, but relatively fixed blockage ratio of approximately 0.5. This provides a uniform plume source flow exiting the honeycomb at the top of the diffuser. The plume issues through two layers of 2.54 cm thick stainless steel honeycomb laid directly on top of a 5.08 cm thick aluminium honeycomb (all with 3 mm nominal cell size). A detailed analysis of the spatial velocity distribution of the plume inlet (average measurement spacing = 0.09 m) shows that the inlet velocity profile (with air instead of helium) is uniform to within 6 % (Blanchat 2001).

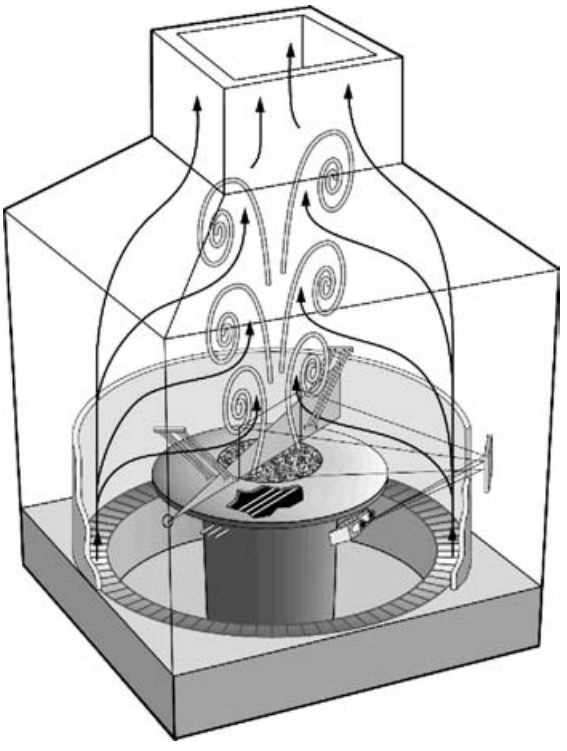

FIGURE 1. Schematic of PIV/PLIF set-up in FLAME facility ($6.1 \times 6.1 \times 7.3\,\mathrm{m}^3$). The excimer laser light sheet bisects the plume inlet surface. Two 35 mm motion picture cameras, one recording the ultraviolet image for PIV, the other the visible image for PLIF, view the plume inlet through a mirror. Seed particle injectors are located in the plume and the surrounding air. Facility details can be found in Tieszen *et al.* (1998).

In these experiments, the plume was developed using helium issuing from the diffuser at an average inlet velocity of $0.325\,\mathrm{m\,s^{-1}}$ (see table 1 for test-to-test details). For PLIF measurements, acetone was used as the fluorescent tracer gas, seeded into the helium flow at 1.7 ± 0.1 vol % In addition, 1.9 ± 0.2 vol % oxygen was added to quench acetone phosphorescence (Lozano, Yip & Hanson 1992). The molecular weight of the helium/acetone/oxygen mixture was $5.45\,\mathrm{g\,mol^{-1}} \pm 2.7$ %. Variation in uniformity of the acetone/helium mixture was checked in a calibration test and was found to be less than 4 %, which was the measurement uncertainty of the technique used. The average mixture Reynolds number was $Re = DV_0/\nu = 3200 \pm 0.6$ %, where D is the diameter of the plume source (1 m), V_0 is the inlet velocity, and ν is the kinematic viscosity of the helium/acetone/oxygen mixture. The average Richardson number was $Ri = (\rho_\infty - \rho_p)gD/(\rho_\infty V_0^2) = 76 \pm 6.5$ %, where ρ_∞ is the external (air) density, ρ_p is the plume fluid density, and g is the acceleration due to gravity. The uncertainties in Re and Ri were estimated based on error propagation from each of their constituent parameters.

3. Experimental techniques

A hybrid analogue/digital PIV/PLIF system was developed and applied to make simultaneous time-resolved velocity and mass fraction measurements in the helium

Run number	Helium inlet Velocity ($m\,s^{-1}$) $\pm$ 1.3 %	Test type	$Re \pm$ 0.6 %	$Ri \pm$ 6.5 %	Measured puffing frequency (Hz)	Puffing frequency (Hz) given by $f = V_0(0.8\,Ri^{0.38})/D$ (Cetegen & Kasper 1996)
20	0.314	PIV	3344	80.57	1.20	1.33
22	0.319	PIV	3300	78.06	1.41	1.34
23	0.303	PIV	3198	86.72	1.36	1.32
25	0.340	PIV/PLIF	3306	68.75	1.53	1.36
26	0.315	PIV	3253	80.20	1.39	1.33
27	0.305	PIV	3242	85.32	1.37	1.32
29	0.352	PIV/PLIF	3256	64.32	1.42	1.37
30	0.337	PIV	3176	70.20	1.19	1.36
32	0.349	PIV/PLIF	3275	65.32	1.42	1.37
36	0.316	PIV/PLIF	2933	79.74	1.41	1.33
10 test average	0.325		3228	75.92	1.37	1.34
4 Favre test average	0.339		3193	69.53	1.45	1.36

TABLE 1. Run conditions and results summary for each of the 10 repeat tests and their averages. Uncertainties listed are $\pm$ one standard deviation.

plume. Image acquisition was performed with high-speed 35 mm film cameras for high spatial resolution imaging with sufficient frame rate to capture the dynamics of the flow. The film images were then digitized at high-resolution to allow fully digital processing. Willert (1996) discusses such PIV systems and their accuracy. Digital cameras, while highly desirable, are not yet available with sufficient combined spatial resolution, acquisition rates and ultraviolet (UV) sensitivity for the present work.

The PIV/PLIF illumination source was a Lambda-Physik Model LPX220i pulsed xenon chloride (XeCl) excimer laser. The laser was run at a pulse repetition frequency of 200 Hz and average pulse energy of 290 mJ at the 308 nm wavelength. The UV wavelength allows pumping of acetone fluorescence in the 225–320 nm band, while simultaneously allowing optical filtering of the PIV signal, i.e. UV light scattered by the seed particles can be recorded while visible light is blocked. The full optical set-up consisted of turning mirrors and light-sheet optics, including a spherical lens (7500 mm focal length) and a cylindrical lens (75 mm focal length) to give the 1 m high sheet typically used. The light-sheet thickness was about 8 mm. Thinner light sheets were tested but gave inferior PIV performance, presumably because of out-of-plane motion. The combination of a finite sheet thickness and an interrogation area for PIV analysis defines a volume within which a statistically most probable velocity representing the bulk motion in the volume is found. This volume sampling is consistent with the interpretation of results from LES numerical simulations.

Two 35 mm Photosonics 6E motion picture cameras were used to collect the PIV and PLIF images, which were acquired simultaneously in order to obtain velocity and mass fraction data on a vertical plane approximately 0.86 m high by 1.2 m wide centred laterally on the plume centreline and extending upward from the plume source to include the core of pure plume fluid, the near-field mixing zones and surrounding air. The plume source is 1 m in diameter so the captured images include the entrainment zones on both sides of the plume. The PIV camera used a quartz UV Nikkor lens with a Schott UG11 bandpass filter (250 to 390 nm bandpass) that allowed the 308 nm PIV signal to be collected while blocking stray sunlight. PIV images were recorded on 61 m rolls of Kodak T-Max ASA 400 35 mm black and white motion picture film. T-Max

film has a wide exposure latitude, extremely fine-grained resolution, and good UV sensitivity. The 200 frame s^{-1} unprocessed PIV images provide excellent visualization of the flow, with an average of 146 images per plume puffing cycle.

In general, for weak excitation, the acetone fluorescence signal $S_f(\lambda, T)$ is given by (e.g. Thurber, Grisch & Hanson 1997):

$$S_f(\lambda, T) \sim X_{acetone} N(T, P) \sigma(\lambda, T) \phi(\lambda, T) I_L, \tag{1}$$

where $X_{acetone}$ is the acetone mole fraction, $N(T, P)$ is the total gas number density, $\sigma(\lambda, T)$ is the absorption cross-section, $\phi(\lambda, T)$ is the fluorescence quantum yield, I_L is the laser energy, T is temperature, P is pressure and λ is the excitation wavelength. For constant T, P and a fixed λ, the fluorescence signal $S_f(\lambda, T)$ is directly proportional to the acetone mole fraction and laser energy. PLIF images were recorded using a second camera with a standard glass lens. Acetone fluorescence was pumped using the 308 nm wavelength of the laser and collected as a broadband signal in the visible wavelength range, from 350–550 nm (Lozano *et al.* 1992). The glass lens acted as a filter to block the UV PIV signal. Since the acetone fluorescence signals were relatively weak, they were collected through an image intensifier (Varo Model 5700, 18 mm diameter, P20 phosphor, with gain approximately 400, and gate width 10 μs) and also captured on 61 m rolls of Kodak T-Max ASA 400 35 mm black and white motion picture film. Above 100 Hz, the intensifier began demonstrating nonlinear behaviour and a substantial decrease in gain. For this reason, the intensifier was run at 100 Hz, still synchronized with the laser and the 35 mm cameras. Therefore, the PLIF film had an image only on every other frame. The alternate frames were PLIF images without an intensifier trigger, and were essentially blank. To aid in normalization of the PLIF images, two additional images were recorded. First, a Kodak HG2000 digital camera recorded the laser beam intensity profile at the time of each exposure. Secondly, prior to each PLIF run, a sequence of images was recorded as the laser sheet passed through a large acrylic calibration box filled with a known, uniformly mixed concentration of acetone in air. Use of these additional images for PLIF processing will be discussed below.

The film cameras were mounted side-by-side for all tests and viewed the plume through a large front surface mirror, as shown in figure 1. During each test, the camera shutter openings were synchronized and controlled the excimer laser pulses so PIV and PLIF frames were captured simultaneously.

The seed particles selected for PIV were glass microballoons (3M Scotchlite K1) with a mean particle diameter of 65 μm and a density of 0.125 g cm^{-3}. Seeding was done both in the plume inlet diffuser and in the room air surrounding the plume. The Stokes-number-based characteristic particle response time was about 1.7 ms for particle motion in air at 20 °C. Given a camera framing rate of 5 ms, this particle response was considered adequate; resolving all the frequencies that the camera could capture, but filtering much of the higher-frequency spectrum that could lower the cross-correlation between the images. The particle settling velocity was approximately 0.015 m s^{-1}, compared to an inlet velocity of 0.35 m s^{-1}. The relatively large particle size was chosen becuse of the need for single particle resolution in the large image area required to capture the near field of the fully turbulent plume. Glass, instead of lower density plastic, was chosen so that simultaneous PIV and PLIF could be performed. Plastic microballoons could not be used because they fluoresced under UV excitation with an emission wavelength in the range of interest for acetone fluorescence (PLIF).

The 35 mm motion picture film images from the Photosonics 6E cameras had a square format (picture size 25 mm wide × 25 mm high) and were digitized at high resolution using a custom film digitizer based on a Photometrics Quantix CCD camera

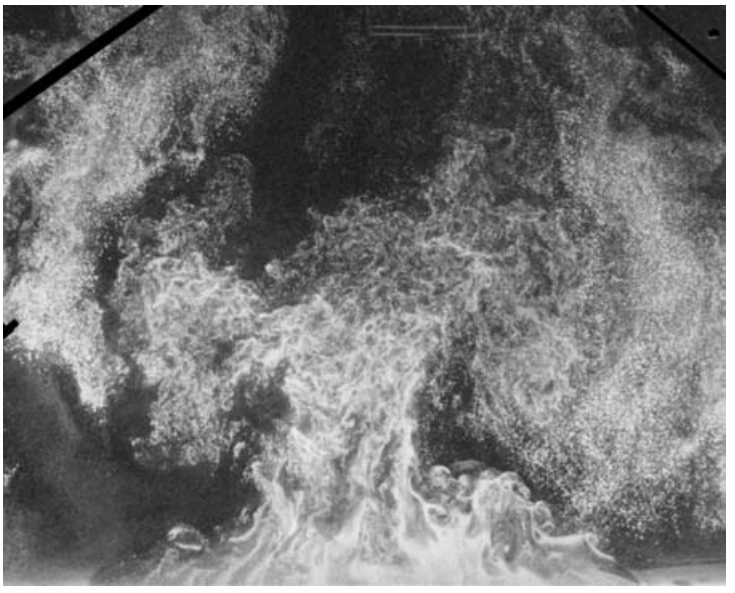

FIGURE 2. Sample raw PIV image in 1 m diameter helium plume (from Test 25).

(2k × 3k, 12 bit). An automated film scanning station used stepper motors to control the film motion and Quantix camera operations. The film was held rigid and flat during digitization. Because of camera vibrations during acquisition and inaccuracies in stepping the film through the digitizer, the digital images were not always perfectly aligned. Therefore, they were later automatically registered to each other prior to PIV or PLIF analysis. This was done by choosing a clearly defined reference point on each image set and applying cross-correlation and image registration features of the ImagePro Plus software package (V. 4.0, Media Cybernetics, Silver Spring, MD). Image registration resulted in ± 1 pixel uncertainty in the spatial alignment of the images, which had a base resolution of 1520 pixels m^{-1}. PIV images were digitized with 8 bit resolution; PLIF images with 12 bit.

4. PIV Analysis

A raw PIV particle field image is shown in figure 2. Two-frame cross-correlation PIV analysis was performed using PIV Sleuth software (Christensen, Soloff & Adrian 2000). PIV Sleuth includes an iterative interrogation capability to extend the dynamic range of the PIV technique. Iterative interrogation is a PIV analysis method that allows offset of the interrogation region, so that particles that have moved out of the interrogation area from one time step to the next can still be cross-correlated. Iterative interrogation is a two-pass process. The first interrogation produces a coarse field of vectors that is much sparser than the desired final field of vectors. The second interrogation uses a finer grid to generate the desired final field of vectors. In the fine-field interrogation, each vector from the coarse field is used to offset the fine-field interrogation window at the corresponding location. Since two fast Fourier transform (FFT) cross-correlations are performed (a coarse and fine), iterative interrogation creates multiple correlation peaks, resulting in highly accurate vectors as well as a very full field of velocity vectors, even when the velocity dynamic range is large. This capability is critical in the current application where, owing to the strong buoyant

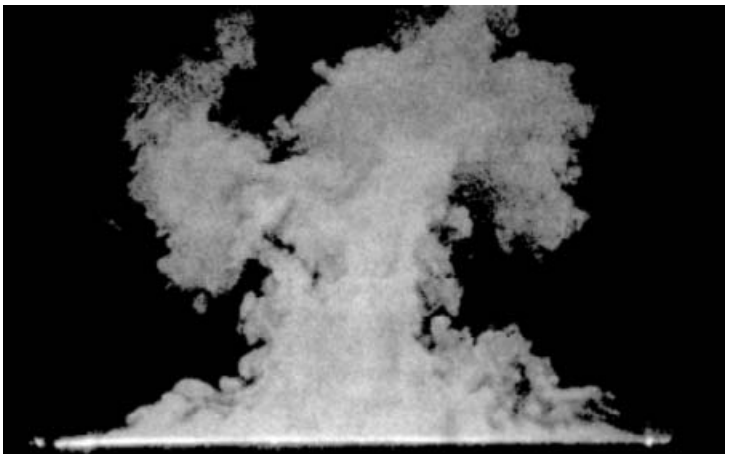

FIGURE 3. Sample raw PLIF image in 1 m diameter helium plume, acquired simultaneously with the PIV image in figure 2.

acceleration in the plume, velocities are found to range from 0.1 m s^{-1} to over 5 m s^{-1} in the same image.

For measurement of the coarse field, two interrogation window sizes were used. The first window size was smaller than the second. The first window searched inside the second window to find the best FFT cross-correlation peak. When the best correlation peak was found, the corresponding velocity vector was placed in the center of the larger second window. For the coarse field of most of the current tests, a first window of 64×64 pixels (4.2 cm) and second window of 128×128 pixels (8.4 cm) was used with 50 % overlap. Test 32 was the exception, with a 128×128 pixels first window used inside a second window of the same size. The coarse field was validated to remove spurious vectors. Typically, 25 % of the vectors were removed during validation. Interpolation allowed replacement of some of the removed vectors, based on the average of a specified number of surrounding vectors. Interpolation (single pass) replaced approximately 60 % of the vectors removed, so that 90 % of the coarse field was filled with vectors.

Fine-grid interrogation was then performed with each coarse-grid vector used as an average to offset each fine-grid independently. The fine field (final) determination used interrogation windows of 32×32 pixels (2.1 cm) with 50 % overlap to generate 10 881 vectors per image pair. Validation typically removed 5 % of the vectors. Interpolation replaced as many as 60 % of the removed vectors, so that 95 % to 98 % of the final field was filled with vectors.

Finally, the 11 500 time planes were temporally (Reynolds) averaged and the statistics were calculated. Note that PIV cross-correlation was performed between each pair of images, e.g. images 1 to 2, 2 to 3, 3 to 4, etc. so that the calculated velocity fields are equally spaced in time (every 5 ms).

5. PLIF analysis

A raw digitized PLIF image as recorded on film during the experiment is shown in figure 3. Quantitative amplitude data must be extracted from the images to determine the mass fraction distribution of plume fluid (mostly helium) throughout the plume. The basic steps in converting the raw film PLIF images to quantitative mass fraction values are: digitization, film and intensifier correction, normalization for laser beam

intensity profile, absorption correction, scaling and spatial averaging. This analysis was performed using Matlab (V. 6.0, The MathWorks, Natick, MA) and ImagePro Plus software. The key steps in the processing are described briefly below.

Step 1. Digitization

To allow quantitative analysis, the raw film PLIF images were first digitized with 12-bit resolution. For each sequence of PLIF images digitized, flat field (image of the digitization illumination source) and dark field (image of dark current arising from the digitization camera over the exposure time) images were recorded. These were used to correct each digitized PLIF image for digitization light source non-uniformity and camera effects. Image registration was performed as for the PIV images.

Step 2. Film and Intensifier Correction

In the next step, it was necessary to relate the film emulsion density to fluorescence intensity, so a calibration that accounts for the film response and image intensifier characteristics was required. Film has a density (transmissivity) proportional to the intensity of illumination under which it was exposed, with the density *vs.* exposure curve having a characteristic logarithmic shape. To simultaneously determine the effects of the intensifier and the film response in the PLIF images, images of a 21-step neutral density filter wedge were recorded. The step wedge had known density ratios of $\sqrt{2}$ between each step. Images of the step wedge were recorded on film under simulated test conditions (e.g. running the intensifier at 100 Hz). Analysis of each wedge image was made to determine an appropriate relation between film emulsion density and incident light intensity. From this, an overall calibration curve was developed and used to convert each raw digitized PLIF image into a new image containing the incident fluorescence signal.

Step 3. Normalization for laser beam intensity profile

The fluorescence signal is proportional to the acetone mass fraction, but it also depends on the laser illumination intensity (as per (1)). The laser beam does not have a uniform intensity profile, so the intensity distribution of each pulse was profiled by splitting off a small portion of the expanding laser beam, directing it to a target, and recording the resulting light intensity distribution using a digital video camera (Kodak HG2000). During PLIF analysis, this beam profile was expanded to produce a synthetic image of the excitation laser sheet, using the optical geometry of the experiment. After correction for flat and dark fields, exposure time, and film and intensifier characteristics (Steps 1 and 2 above), each PLIF image was divided by its corresponding laser sheet intensity profile to correct for the excitation intensity distribution and its shot-to-shot variations. The geometry and expansion characteristics of the normalization beam were confirmed using images of the laser beam expanding into a uniformly mixed acetone-filled calibration box that were recorded immediately prior to a helium plume test.

Step 4. Absorption correction and data scaling

Since laser energy was absorbed by the acetone, the fluorescence intensity drops off by as much as 50 % from the laser side to the opposite side of the plume. A correction for the absorption was made by marching along each ray of the expanding laser sheet in vertical planes beginning at the laser inlet side of the plume. The PLIF intensity was corrected to that which would have been present if there had been no attenuation using the exponential correction for transmissivity as a function of concentration, path length and absorption characteristics of the light-attenuating medium. Single and multiple iterative pass corrections were tried with only small variations in the

final results once the appropriate absorption coefficients were determined. Data for the absorption coefficients were determined using images of the calibration box since it contained a uniform known acetone concentration. Following absorption correction, relative acetone mass fractions were determined by scaling the maximum PLIF intensities at the plume source to absolute mass fraction values using the known mass fraction of acetone at the plume inlet, i.e. 1.7 vol % in this case. This distribution was linearly converted to relative mass fraction of plume fluid, assuming perfect mixing between the acetone, helium and oxygen.

Step 5. Spatial Averaging

The previous steps yielded mass fraction values at each pixel within the PLIF image. Spatial averaging was performed to provide a value of mass fraction averaged over the same (2.1×2.1 cm) spatial extent as the PIV interrogation area. This allows consistent joint statistics to be calculated for each interrogation area over the full field of the plume. We estimate the Batchelor scale to range from 0.5 to 0.8 mm for these gases and flow conditions, based on measured velocity fluctuations and handbook values of gas properties. The full resolution PLIF data are able to resolve this scale as each pixel in the PLIF images corresponds to 0.5 mm. However, all of the concentration results presented in this paper are average intensity values over a 2.1×2.1 cm region (approximately 40×40 pixels) to yield an average concentration value over the same resolution as the PIV images. These consistent velocity and concentration fields were required in order to perform the Favre statistics calculations. The full resolution data sets are available, but have not been included in this paper.

As a final check on the consistency of the results, the calibration box images, which contained known, uniform acetone concentrations in air, were used to check each of the PLIF analysis steps to assure that they gave uniform corrected PLIF images for each box.

5.1. *Simultaneous PLIF and PIV considerations*

To obtain the desired PIV images, it is necessary to use seed particles that scatter the laser light which is pumping the fluorescence signal. If the seeding density is uniform, or the light scattered by seed particles is only a small fraction of the incident light, then there is little adverse interaction between the PIV and PLIF diagnostic techniques (given the spectral separation of the signals). Considerable effort was made to achieve PIV seeding with sufficient uniformity and density to provide a full PIV field and yet minimize adverse interactions with the PLIF measurements. Adverse interaction expressed itself in the PLIF images as dynamic striations indicating relatively denser seed loading moving with the flow. Of the 10 tests conducted and analysed using PIV, four were found to have minimal striations present and were therefore analysed for PLIF.

The data from the simultaneous PIV and PLIF diagnostics permit density (Favre) weighted time-average statistics to be calculated. Because the PLIF was analysed for only four of the ten tests, and the density field has only half the framing rate, the resultant Favre-averaged statistics contain nominally only 20 % of the data of the Reynolds-averaged statistics shown. Also, owing to intensity requirements for the PLIF signal, data could not be reliably obtained for all tests above an axial elevation of 0.76 m so joint statistics are limited to this elevation and below.

6. Error analysis

The velocity values determined using PIV are dependent on accurate measurement of the time period between images, a physical scale for determining particle

displacement during that time period, and accurate frame-to-frame registration (so that a stationary object would be measured as having zero velocity). Error sources can also arise during the cross-correlation analysis, including improper choice of correlation peak, effects of out-of-plane motion, velocity gradients, etc. These errors were minimized as follows. The camera timing was recorded on a high-speed data trace, allowing determination of the image separation period to within better than 1 %. The physical scale was determined from several known markers in each image. This measurement was repeated several times and was repeatable to within less than 1 %. Frame-to-frame registration was done by cross-correlation of fixed objects in the field of view, introducing ± 1 pixel displacement uncertainty. A 'jitter' correction was later performed on the PIV vector field in a small number of images, to eliminate constant velocity shifts throughout the velocity field, which presumably arise owing to improper image-to-image registration. Using a thick light sheet minimized out-of-plane errors. Beam steering effects caused by the fluctuating density gradients between the illuminated plane and the cameras were found to be negligible. Beam steering was checked by placing a calibrated grid along the centreline of the helium plume with helium flowing and ensuring that the recorded images showed no motion of the grid. The final values of velocity contain uncertainties on the order of ± 20 %. The turbulent statistics contain uncertainties on the order of ± 30 %. These uncertainties are higher than those normally associated with PIV (e.g. Megerle, Sick & Reuss 2002) for several reasons. (i) The ± 1 pixel displacement due to registration could lead to ± 3.1 % uncertainty. (ii) The $2.1\,\mathrm{cm} \times 2.1\,\mathrm{cm}$ interrogation region, while relatively small compared to the large PIV field, could encompass velocity gradients and thereby cause gradient effects such as statistical bias toward lower velocity and poorer correlation (Keane & Adrian 1992). This interrogation area was found to be the best compromise for yielding valid velocity vectors over the entire flow field, allowing batch PIV processing with constant analysis parameters. (iii) It was difficult to maintain uniform PIV seeding throughout the entire field (see figure 2) so some vectors were determined based on sparse particle fields or were interpolated during filtering and smoothing. As mentioned above, typically 25 % of the coarse field vectors were removed and replaced during PIV validation. (iv) Most importantly, the PIV uncertainty encompasses effects of run-to-run experimental variations.

The acetone mass fraction profiles as determined using the PLIF technique described above are subject to error sources involved with image registration, film response correction, laser sheet intensity normalization, mass fraction calibration and absorption correction. Registration errors are comparable to those described above for the PIV analysis. A main portion of the uncertainty in the PLIF analysis arises from the correction of the images for the nonlinear response characteristics of the film and image intensifier combination. However, based on intensive analysis of multiple step wedges and calibration box images, the film-intensifier response calibration was captured to within ± 5 %. Because of the coupling of laser sheet generation, normalization and absorption correction steps in the PLIF analysis, the individual errors arising from each of these steps are difficult to quantify at the present time. They were assessed via consistency and calibration checks undertaken throughout the PLIF analysis and were minimized where possible. Based on the results, it is estimated that final values of the mass fraction embody uncertainties of the order of ± 18 % of the measured mass fraction plus a fixed offset of up to ± 5 %. The fluctuating mass fraction data contain uncertainties of the order of 21 %. Again, the most important source of overall uncertainty in these experiments arises from test-to-test experimental variations.

7. Experimental approach

The test procedure was to start the flow of the helium mixture (helium with acetone vapour and oxygen), allow several minutes of flow to establish stable conditions, initiate seed particle release, and then several seconds later start the cameras, which ran for about 8 s for a 61 m film roll. For each test, inlet, outlet and boundary measurements were made to characterize mass, momentum and energy initial and boundary conditions. The boundary condition diagnostics included velocity, temperature and humidity in the air inflow ducts; static and differential pressures throughout the facility; and mass flow rate in the gas supply lines. Including timing channels (start, camera shutters and laser pulses), the data acquisition system recorded 30 channels per test. Full data sets are available upon request from the authors.

8. Data analysis and results

In contrast to a momentum-driven jet flow, the plume in the current study has a very low initial velocity of $0.325\,\mathrm{m\,s^{-1}}$. The 3 mm diameter cells in the source honeycomb further suppress turbulence in the inlet flow. Flow visualization movies, from which figures 2 and 3 have been extracted, strongly suggest that the helium mixture inflow conditions are laminar. Air entrainment velocities are also low and visualization suggests weak turbulence in the air owing primarily to the overall puffing behaviour of the plume. In spite of these nearly laminar flow conditions, visualization shows that strong turbulent structures form at the interface between air and the helium mixture (see figures 2 and 3) as close as a few centimetres from the plume source. The lack of source turbulence, and the strong deflection of the low-velocity helium plume from vertical at the edges of the source, suggest that vorticity from the source boundary layer is not responsible for the formation of these turbulent structures at the helium–air interface, rather that they are formed by buoyancy-driven (gravitational and baroclinic) vorticity generation. Regardless of the cause, it is clear from the density field in figure 3 that flow structures with a range of length scales exist and the plume can be considered fully turbulent.

Figure 4 shows a single snapshot of the velocity field as determined by PIV analysis of one image pair. At this instant, plume development is characterized by the two counter-rotating vortices (a planar cut through a toroidal vortex structure) at about $y = 0.45$ m above the inlet, with plume necking and entrainment evident below this vortex. PIV analyses were conducted on approximately 11 500 images from the helium plume, covering 70 puff cycles of the flow, while PLIF analyses were performed on approximately 2300 images, covering 33 puffs. Recall that the PLIF data were recorded at 100 Hz, while PIV was recorded at 200 Hz. PLIF data were analysed only for four of the ten tests used in the PIV analysis. The data will be discussed from two perspectives, first from a qualitative turbulent dynamics perspective that identifies the source and interaction of two turbulence modes and second from a quantitative time-averaged perspective that presents both Reynolds- and Favre-averaged results.

8.1. *Turbulent plume dynamics*

Large-scale turbulent dynamics is dominated by 'puffing'. Figure 5 shows the time trace of vertical velocity at a point on the plume centreline, 0.5 m (1/2 plume diameter) above the inlet. Figure 5 clearly shows variations in the vertical velocity for 8 cycles that correspond to the passage of large coherent turbulent structures. As noted, the flow is fully turbulent so the structures are not exactly periodic, but often consist of

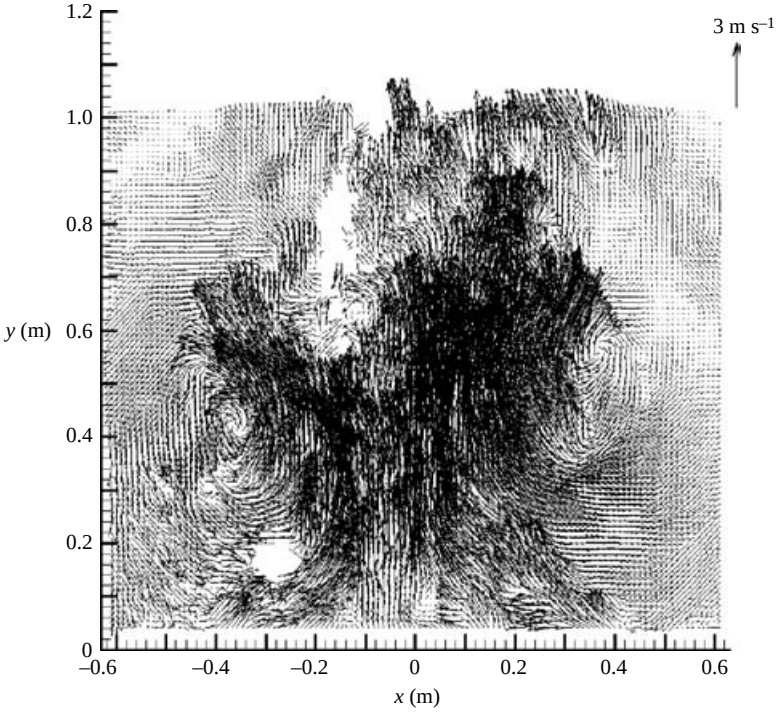

FIGURE 4. Instantaneous PIV velocity field in the helium plume acquired from image in figure 2 and a second image acquired 5 ms later. Missing vectors indicate inadequate local seeding.

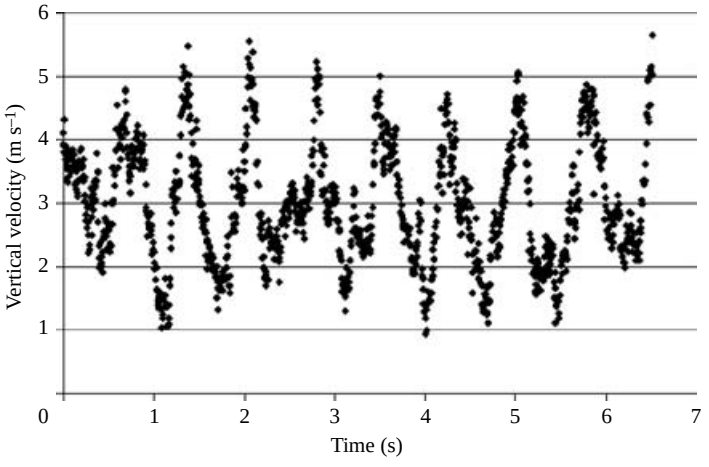

FIGURE 5. Time trace of PIV vertical velocity vectors at the location $x = 0.5$ m, $y = 0.5$ m in Test 23. The passage of 8 quasi-periodic puff cycles is clearly seen.

fairly uniform puffs separated by an occasional weaker puff. Note that similar time histories to that shown in figure 5 exist for every vector shown in figure 4.

Puffing of turbulent plumes has been described in many previous investigations (e.g. Cetegen & Ahmed 1993; Cetegen & Kasper 1996; Soteriou, Dong & Cetegen 2002). The key observations will be summarized here. As light plume fluid exits the plume inlet, it slowly accumulates until it reaches sufficient volume to trigger

a Rayleigh–Taylor instability caused by a heavy fluid overlying a lighter fluid. The lighter plume fluid then bursts upward as a large toroidal vortex, with a diameter approximately equal to that of the plume inlet. As the vortex rises, it entrains air below it and accelerates upwards, narrowing the plume fluid below it down to a thin 'neck'. The neck then begins to thicken until another volume of buoyant fluid is accumulated and the cycle repeats. The average puffing frequency determined by timing the peaks of the velocity traces in the 70 puff events analysed here is 1.37 Hz. This frequency, f, is in good agreement with the Cetegen & Kasper (1996) correlation suggested for $Ri < 100$, $f = V_0(0.8Ri^{0.38})/D$, where V_0 is the inlet velocity, Ri the Richardson number, and D the plume base diameter, which predicts a puffing frequency of 1.34 Hz. The frequency predicted by this correlation for each of the tests is also shown in table 1. The data are also in general agreement with the Cetegen & Ahmed (1993) correlation for buoyant diffusion flames of various fuels, $f = 1.5D^{-0.5}$, which predicts a puffing frequency of 1.5 Hz, independent of flow conditions.

The temporal and spatial resolution of the current data set permit a second turbulence mode to be identified and tracked in addition to the puffing mode. Figure 6 shows the growth of both the large coherent vortex, characteristic of the puffing, and the growth of smaller-scale classical Rayleigh–Taylor (RT) bubble and spike structures. Growth of the smaller scale RT structures precedes the growth of the coherent large-scale vortex associated with puffing. Figure 6(a) shows an instantaneous PLIF image that will represent an arbitrary time zero reference for the images that follow. All images in figure 6 are cropped to the left-hand half of the plume to focus on the dynamics near the base. In figure 6(a), the large coherent puff is leaving the top of the image. As the vortex is self-advected downstream, the velocity field induced by that large vortex near the surface of the plume begins to weaken and helium begins to flow vertically upward from the plume source. Figures 6(a), 6(c), 6(e), 6(g), 6(i) and 6(k) represent time planes separated by 1/6 of a puff cycle. The seventh image (figure 6m) represents the start of the next cycle. The large vortex which characterizes the puff is represented in figures 6(a), 6(c), 6(e), 6(g), 6(i) and 6(k) by a circle with arrows to clarify the image. Similarly, the growth of the classical RT bubble and spike structures which characterize the second mode is represented by the straight arrows.

The corresponding turbulent momentum field is best illustrated by the difference between the instantaneous velocity vector fields and the time mean velocity vector field shown in figure 7(a). Figures 6(b), 6(d), 6(f), 6(h), 6(j), 6(l) and 6(n) show the instantaneous vector fields minus the time mean velocity field that correspond to PLIF images in figures 6(a), 6(c), 6(e), 6(g), 6(i), 6(k) and 6(m), respectively. Superimposed on the turbulent momentum fields are the contours of the instantaneous plume edge. In figure 6(b), the large coherent structure can be seen in the upper half of the image by noting the upward velocity vectors near the plume centreline (right-hand side of image) and the downward vectors outside of the plume (left-hand side of image). It is clear that this vortical structure is centred on the large scalar helium 'puff' shown in figure 6(a). The effect of the vortex on the velocity field is seen in the lower half of the image in which the instantaneous velocity is downward and radially inward relative to the time mean velocity. In figures 6(a) and 6(b) helium is beginning to push its way upward from the plume source at the bottom of the image. In figure 6(b), the velocity vectors in the region of the helium upflow are still down and radially inward relative to the mean upflow shown in figure 7.

Progressing in time through figures 6(c–d) and 6(e–f), it can be seen that the helium continues to rise from the plume source as the coherent vortex leaves the domain at the top of the image. In the bottom half of the images, helium 'bubbles'

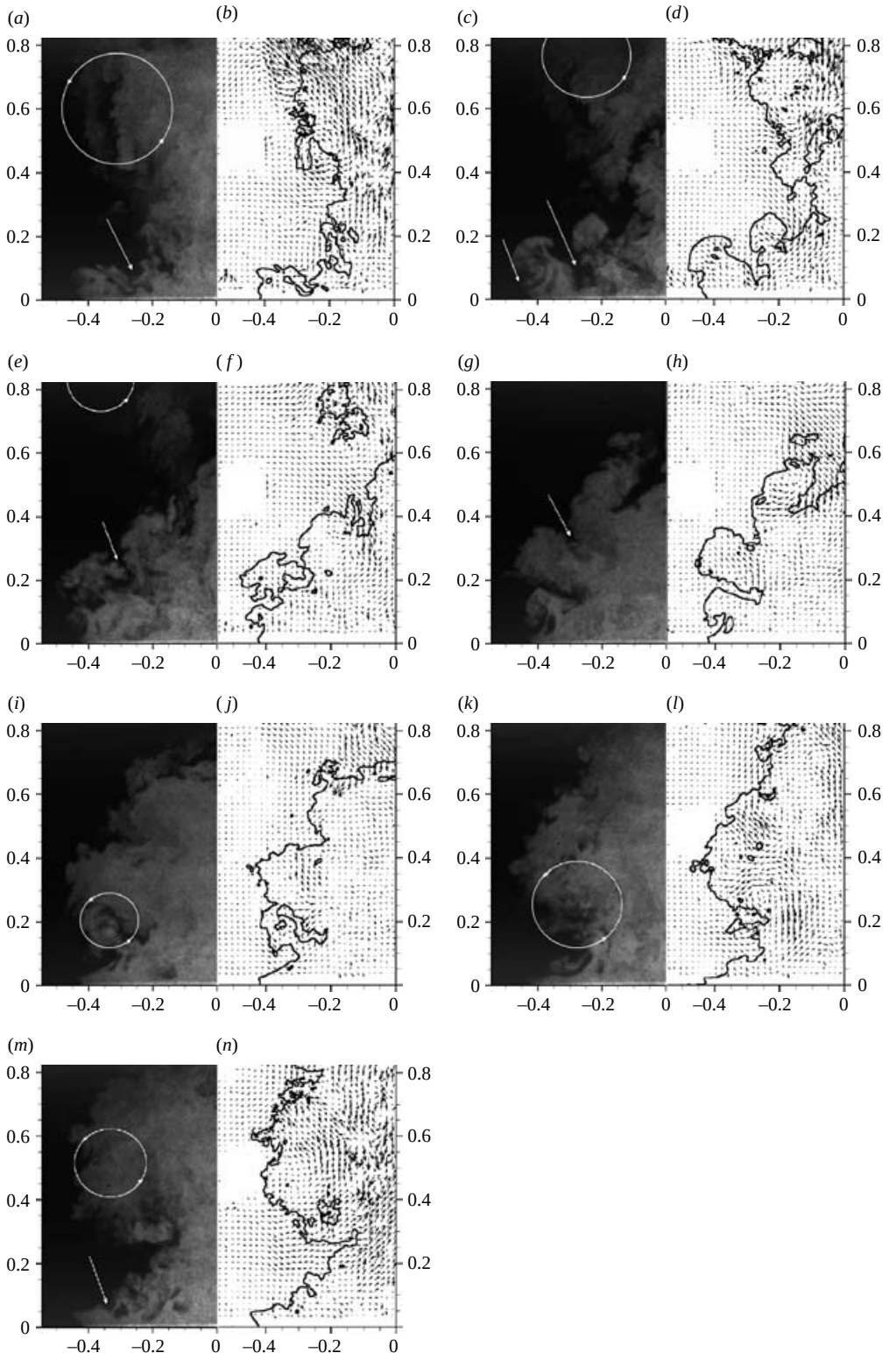

FIGURE 6. For caption see next page.

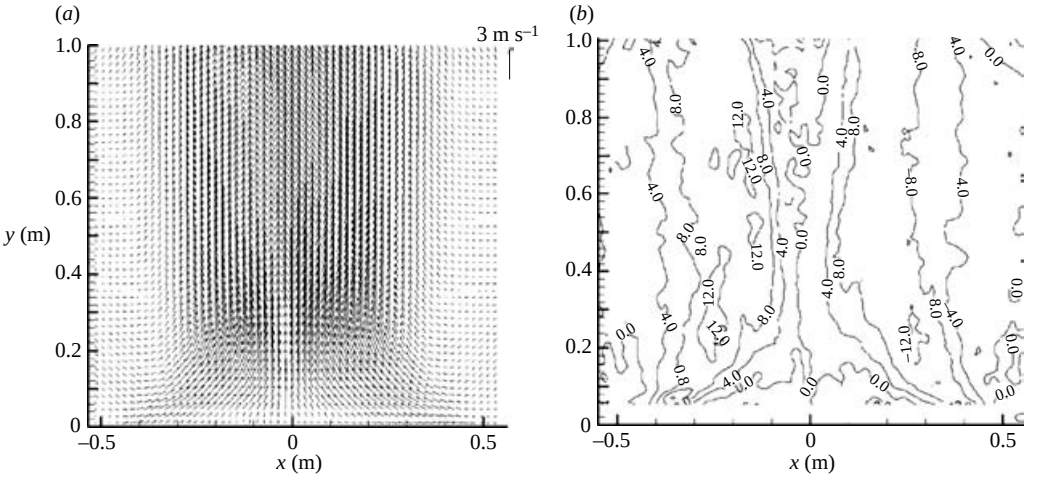

FIGURE 7. (*a*) Time-averaged PIV velocity field in the helium plume based on 11 500 images (70 puff cycles). Only every second vector in each direction is shown for clarity. (*b*) Time-averaged vorticity field computed from the velocity field in (*a*).

and air 'spikes' can clearly be seen growing. These classical RT structures are due to the heavy air overlying the light helium. The air overlies the helium owing to the radial entrainment of air over the inflowing helium by the coherent vortex associated with the puffing. Within the RT bubble and spike structure, velocity differences between the upflowing helium bubbles and downflowing air spikes are clearly evident (keeping in mind that the mean velocity field has been subtracted from all the vectors so that the upflow of the helium bubbles is at near neutral velocity and the air spikes are strongly downward). In addition to growing, the RT structures cause significant mixing of the helium and air. By the time the plume is half-way through the puff cycle, the helium and air have become significantly mixed near the source, as can be seen in figure 6(*g–h*).

The growth of the coherent vortex associated with puffing can be inferred from the conditions shown in figure 6(*e–f*). If the plume source were infinite in spatial extent with no edge effects, then it would be expected that classical RT structures would exist over the full extent of the interface. However, the plume source here is finite −1 m in diameter. In figure 6(*e–f*), it can be seen that the helium has pushed to a significant extent into the air above the inlet. Mixing of the air and helium has produced a disk-like layer of helium/air mixture above the plume source. There now exists a horizontal density gradient between the helium/air mixture above the plume source and the air adjacent to it. This misalignment of the density gradient with gravity will produce vorticity at the edge of the plume. Unlike the classical RT bubble

FIGURE 6. Left-hand images are instantaneous PLIF mass fraction field in the helium plume; right-hand images are the corresponding PIV vector field overlaid with the general plume outline. Data are approximately 115 ms apart (nominally every twenty-third frame from an acquisition sequence). In the left-hand images, the development and movement of the large toroidal vortex in a puffing event are indicated by circular arrows, and the spike and bubble structures characteristic of the Rayleigh–Taylor instability are indicated by straight arrows. Only every other velocity vector in each direction is shown for clarity. The square of missing vectors is due to calibration light box in raw PIV images blocking the view of that portion of the flow.

and spike structures, this vorticity is not counterbalanced by an adjacent bubble or spike since it is on the edge of the plume. As a result, it forms a vortex which grows in size until it reaches the plume centreline as can clearly be seen in figures 6(*g–h*), 6(*i–j*), 6(*k–l*) and 6(*m–n*).

The condition in figure 6(*e–f*) can be considered to be a special form of the classical Rayleigh–Taylor instability problem. Instead of gravity normal to an interface with a heavy fluid over a light fluid, the finite plume edge clearly represents a condition in which gravity is parallel to an interface with a heavy fluid adjacent to a light fluid. This imbalance of forces results in the formation of a large coherent vortex which grows until it saturates by impinging on a geometric boundary (in this case the centreline of the plume). In this sense, the source of the puffing instability is absolute, and not convective as discussed by Soteriou *et al.* (2002).

The resultant velocity field from this large vortex results in a large radial indraw of air over the helium upflow, effectively deflecting it to nearly the centreline of the plume. The sharp angle of the helium/air interface can clearly be seen in figure 6(*k–l*) relative to figure 6(*e–f*). As this large coherent vortex self-advects upward, the near-source radial velocity field is reduced and once again helium upflows against air and the puff cycle repeats, first with classical bubble and spike structures, followed by the roll-up and self-advection of the edge vortex. The puff cycle in figure 6 is typical of the data, with one exception. This particular cycle has spike structures which are perhaps twice as wide as typical spikes and are therefore resolved enough to be seen in these small-scale figures.

Early transient numerical simulations of this data set (DesJardin *et al.* 2004; Tieszen *et al.* 2004*b*) show that both turbulence modes are important to the time-averaged statistics to be discussed in the next section. Because the RT air spike structures are small-scale features, the numerical studies show that obtaining a grid-converged solution will be very costly. With poor spatial resolution, simulations indicate that the smaller-scale bubble and spike structures are suppressed and only the large scale growth of the edge vortex that results in puffing is resolved. Mean statistics are strongly affected by the lack of mixing owing to under-resolution of the bubble and spike structures resulting in an overshoot of a factor of two in vertical centreline velocity.

8.2. *Reynolds- and Favre-averaged data*

Figure 7 shows the ensemble average of all 11 500 PIV image pairs processed. Figure 7(*a*) shows the time-averaged velocity field, and figure 7(*b*) shows the time-averaged vorticity field. Evident is the overall buoyant acceleration of the plume and resulting air entrainment near its base. It can be seen in figure 7(*a*) that the mean velocity field is nearly symmetric. Figure 7(*b*) shows that the peak vorticity occurs low in the plume near the time-averaged plume–air interface. Figure 8 shows the ensemble-averaged plume fluid mass fraction calculated from the 2300 PLIF images recorded simultaneously with the PIV images used to obtain the mean velocity field (figure 7*a*). High mass fractions of plume fluid are evident on the plume centreline immediately above the surface of the diffuser. These decrease rapidly with elevation and in the radial direction owing to strong entrainment and mixing with ambient air.

Figures 9(*a*) and 10(*a*) show contour plots of the Reynolds (time)-averaged horizontal ($\bar{u}$) and vertical ($\bar{v}$) velocity components. The horizontal velocity contours (figure 9*a*) show strong air entrainment and horizontal velocity gradients near the plume base, with continuing but weaker entrainment at higher axial locations. Note the change in character of the flow above and below the band $0.1 < y/D < 0.2$, as

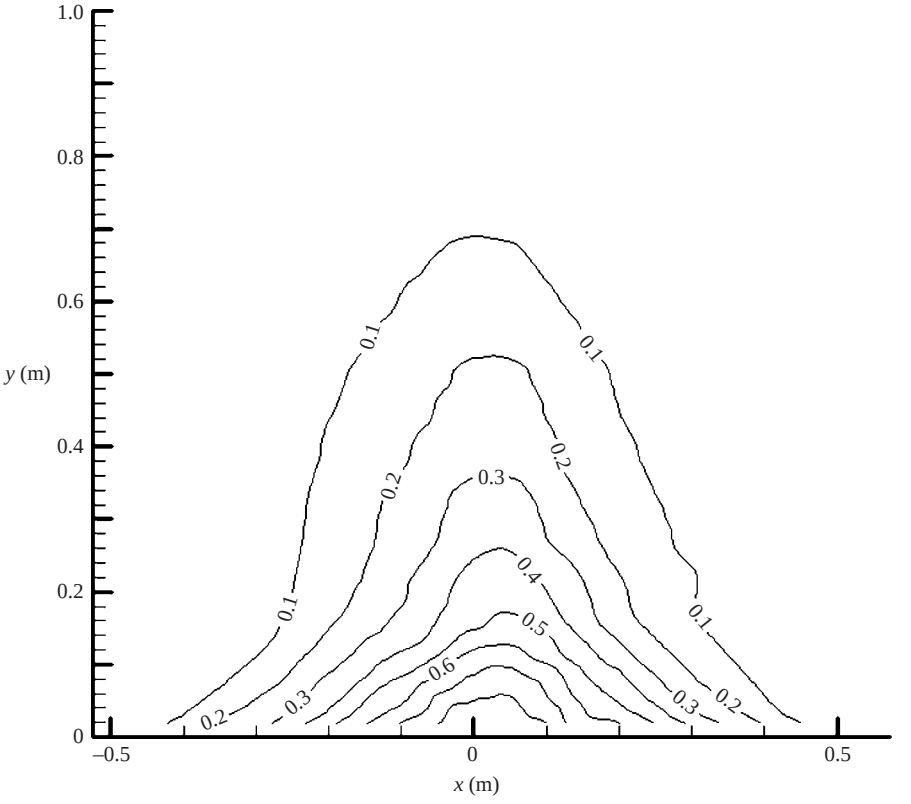

FIGURE 8. Favre-averaged field of plume fluid mass fraction based on approximately 2300 PLIF images (33 puff cycles).

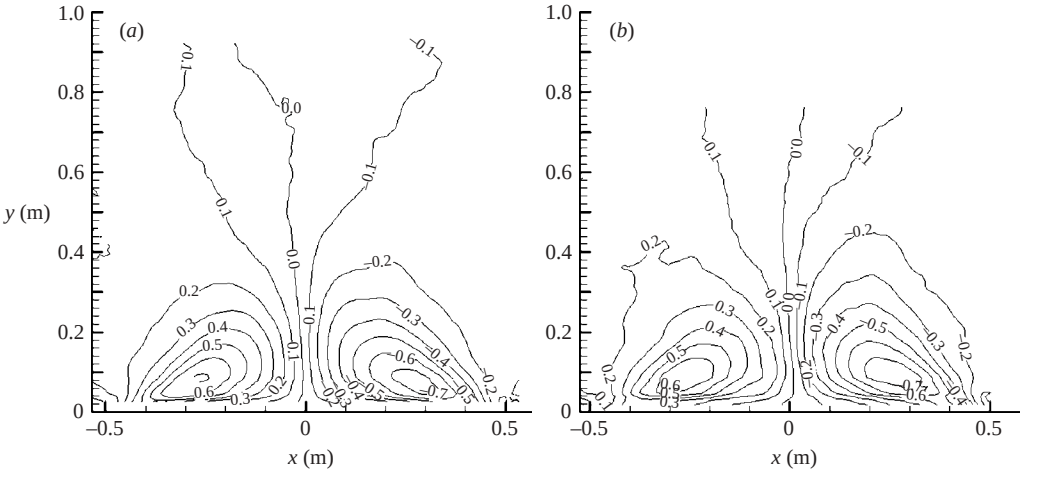

FIGURE 9. Time-averaged horizontal velocity contours. (*a*) Reynolds averaged $\bar{u}(\mathrm{m\,s^{-1}})$, (*b*) Favre averaged $\tilde{u}(\mathrm{m\,s^{-1}})$. The Favre-averaged field extends only to $y = 0.76\,\mathrm{m}$ because that is the extent of the plume fluid mass fraction data.

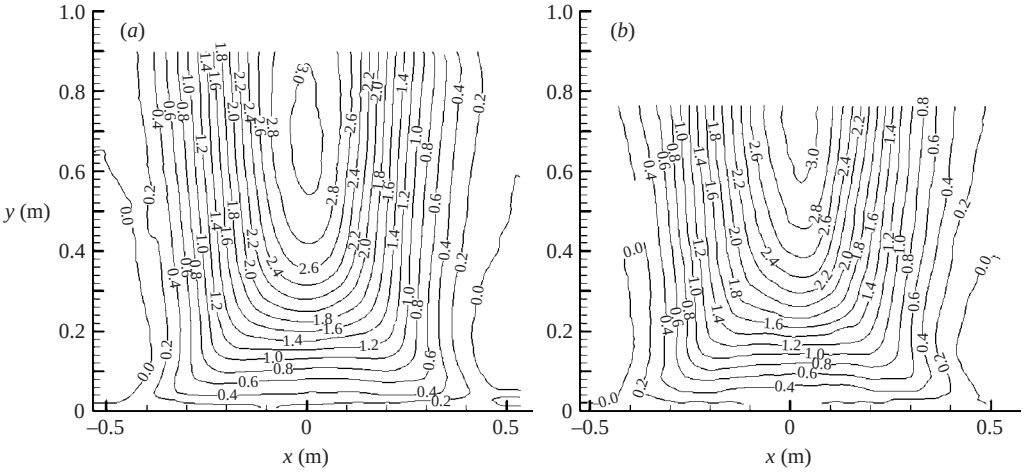

FIGURE 10. Time-averaged vertical velocity contours. (*a*) Reynolds averaged $\bar{v}\,(\mathrm{m\,s^{-1}})$, (*b*) Favre averaged $\tilde{v}\,(\mathrm{m\,s^{-1}})$. The Favre-averaged field extends only to $y = 0.76\,\mathrm{m}$ because that is the extent of the plume fluid mass fraction data.

seen in the horizontal velocity (figure 9*a*), change in radial slope of the mass fraction profile (figure 8) and in the vorticity field (figure 7*b*). All indicate that the helium core has fully collapsed by this elevation. This very rapid collapse of the potential core is starkly different than that observed in constant-density jet flows. The vertical velocity contours (figure 10*a*) show strong symmetric acceleration in the axial direction. The vertical velocity gradients are strongest along the time-averaged plume edge (see figure 7). Good symmetry is seen in the velocity data, except higher in the plume where the horizontal velocity values are very low. Of interest for computational fluid dynamics and validation, the Favre-averaged values $\tilde{u}$ and $\tilde{v}$ are also presented (figures 9*b* and 10*b*), calculated as:

$$\tilde{u}_i = \frac{\displaystyle\int_0^\tau \rho(t, x_k) u_i(t, x_k)\,\mathrm{d}t}{\displaystyle\int_0^\tau \bar{\rho}\tau}, \quad \bar{\rho}\tau = \int_0^\tau \rho(t, x_k)\,\mathrm{d}t, \tag{2}$$

where ρ is the local density derived from the PLIF mass fraction data, u_i the local velocity, t is time, x_i is position, and τ is the time duration of the experiment. Note that other Favre averages presented below were calculated through a process similar to (2).

Figures 9 and 10 show little difference between the Reynolds- and Favre-averaged results, as will be discussed later in the paper. As expected, the differences are most noticeable in regions of high-density gradients. One reason for some of the difference between the Reynolds- and Favre-averaged results is that, as shown in table 1, data from all ten tests were used to compute the Reynolds-averaged statistics, but data from only four of those tests could be used to compute Favre averages. Because of this, the average inlet and boundary conditions for the Reynolds and Favre tests vary slightly. For example, the ten tests used for Reynolds-averaged statistics had an average inlet velocity, Re and Ri of $0.325\,\mathrm{m\,s^{-1}}$, 3228 and 75.92, respectively, while the four tests used for Favre-averaging gave $0.339\,\mathrm{m\,s^{-1}}$, 3192 and 69.53, respectively.

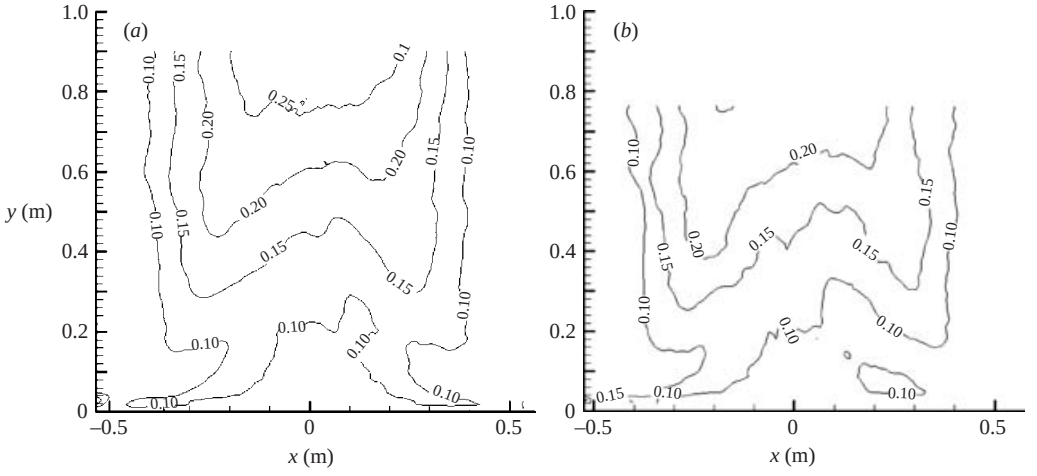

FIGURE 11. Horizontal turbulent normal stress contours. (*a*) Reynolds averaged $\overline{u'^2}$ ($m^2\,s^{-2}$), (*b*) Favre averaged $\overline{\rho u''^2}/\overline{\rho}$ ($m^2\,s^{-2}$). The Favre-averaged field extends only to $y = 0.76$ m because that is the extent of the plume fluid mass fraction data.

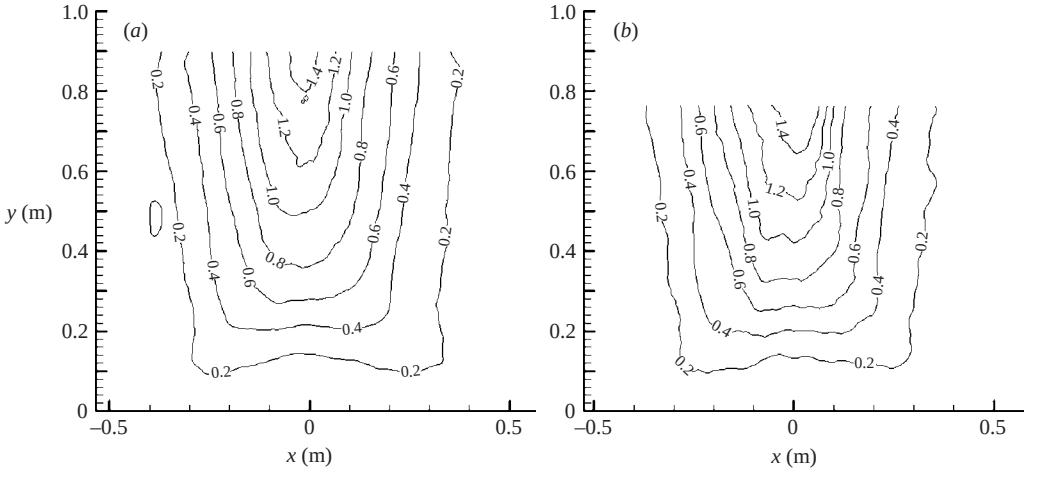

FIGURE 12. Vertical turbulent normal stress contours. (*a*) Reynolds averaged $\overline{v'^2}$ ($m^2\,s^{-2}$), (*b*) Favre averaged $\overline{\rho v''^2}/\overline{\rho}$ ($m^2\,s^{-2}$). The Favre-averaged field extends only to $y = 0.76$ m because that is the extent of the plume fluid mass fraction data.

These small differences were due to slight run-to-run variations in the inlet valve settings and other uncontrolled experimental settings.

Figures 11 to 14 present turbulent statistics derived from the fluctuating velocity fields, specifically the horizontal turbulent normal stress $\overline{u'^2}$, the vertical turbulent normal stress $\overline{v'^2}$, the inplane Reynolds stress $\overline{u'v'}$, and an estimate for the turbulent kinetic energy k, respectively. The individual in-plane stresses are useful for validation of Reynolds-stress turbulence models and for estimation of turbulent kinetic energy production. Figure 11 shows that the highest horizontal turbulent normal stress $\overline{u'^2}$ occurs higher in the plume where the horizontal velocity gradients are small, but the vertical velocity gradients are large. Figure 12 shows similar behaviour for the vertical turbulent normal stress $\overline{v'^2}$. As expected, the inplane Reynolds stress

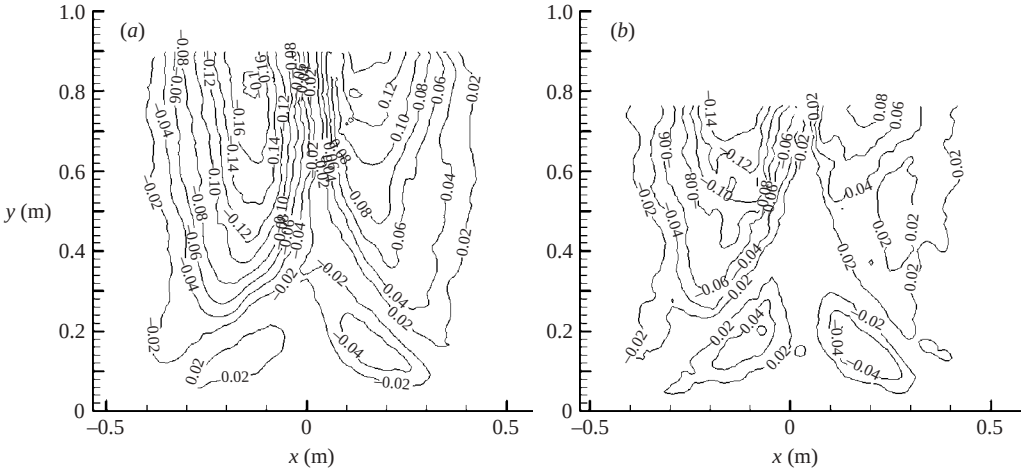

FIGURE 13. In-plane Reynolds stress contours. (*a*) Reynolds averaged $\overline{u'v'}(\mathrm{m^2\,s^{-2}})$, (*b*) Favre averaged $\overline{\rho u'' v''}/\overline{\rho}\,(\mathrm{m^2\,s^{-2}})$. The Favre-averaged field extends only to $y = 0.76\,\mathrm{m}$ because that is the extent of the plume fluid mass fraction data.

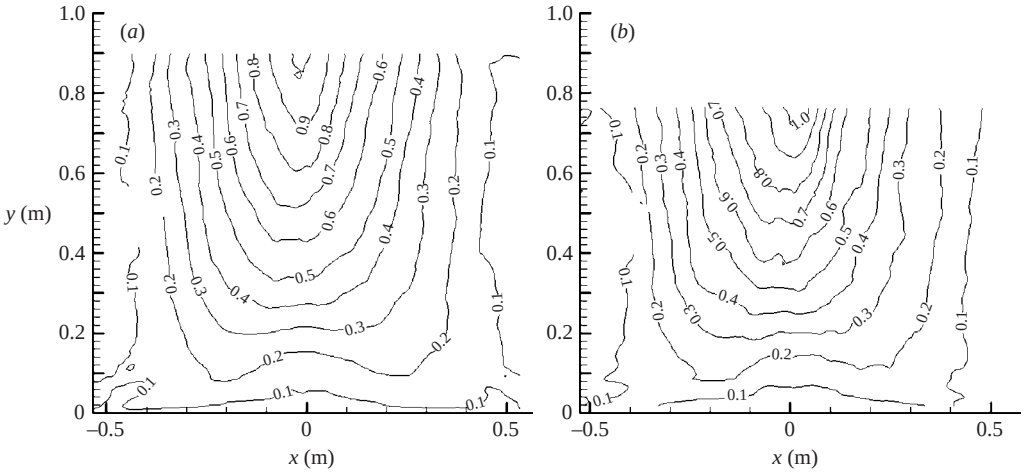

FIGURE 14. Estimated turbulent kinetic energy k contours. (*a*) Reynolds averaged $(\mathrm{m^2\,s^{-2}})$, (*b*) Favre averaged $(\mathrm{m^2\,s^{-2}})$, assuming that the unmeasured out-of-plane turbulent fluctuations are equal to the in-plane turbulent fluctuations. The Favre-averaged field extends only to $y = 0.76\,\mathrm{m}$ because that is the extent of the plume fluid mass fraction data.

(figure 13) shows peak values in the regions of highest gradient in the vertical velocity. For the k–ε models, a measure of the turbulent kinetic energy, k, is needed. The turbulent kinetic energy is the sum of the normal stresses in the three directions. Since the current study conducted in-plane two-dimensional PIV, the out-of-plane normal stress is not known; however, it is not zero. From images of visible methane fire emission, acquired under similar test conditions, it is clear that the vortical structures form from the initiating flow structures in a three-dimensional fashion, resulting in out-of-plane fluctuations. Streamwise vorticity forces tangential rollers at the circumference of the plume to transform into three-dimensional mushroom-cap-like structures immediately. While there is no *a priori* reason to assume that the

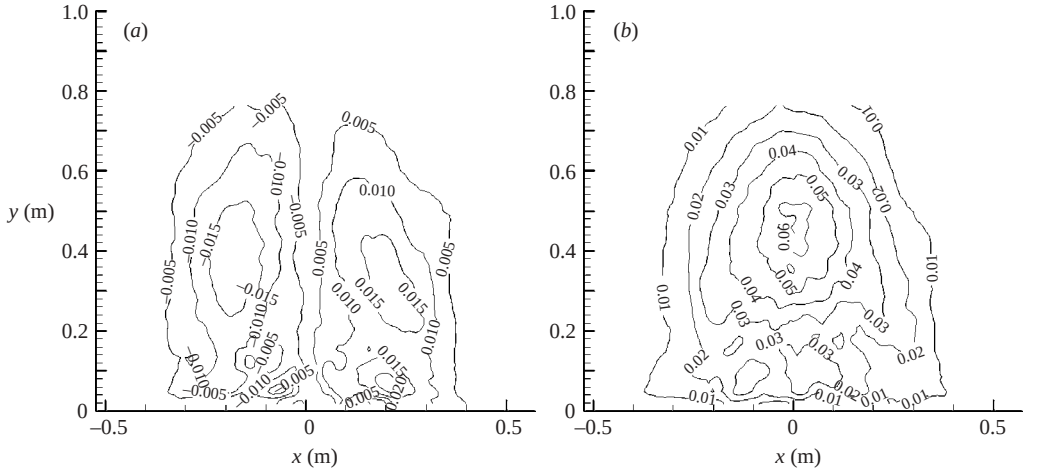

FIGURE 15. Turbulent fluxes. (*a*) Horizontal velocity and plume fluid mass fraction correlation $\overline{\rho u'' Y_p''}/\overline{\rho}$ (m s^{-1}), (*b*) vertical velocity and plume fluid mass fraction correlation $\overline{\rho v'' Y_p''}/\overline{\rho}$ (m s^{-1}).

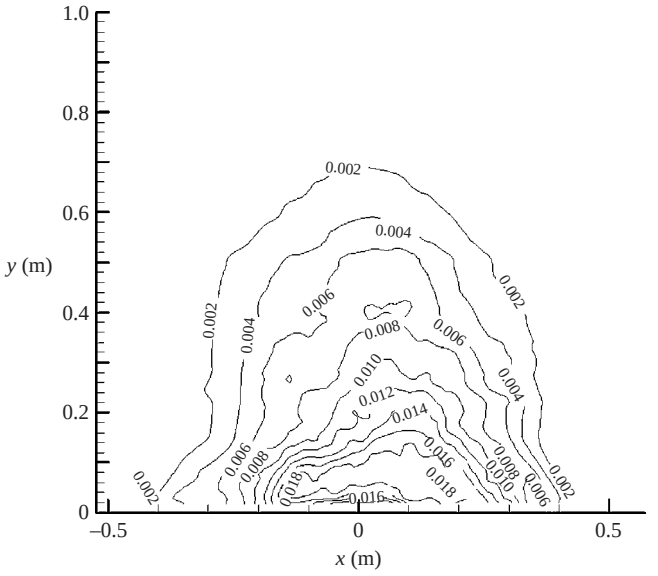

FIGURE 16. Scalar variance–plume fluid mass fraction self-correlation $\overline{\rho Y_p''^2}/\overline{\rho}$.

strength of the streamwise and tangential vorticity is the same, a common assumption made in determining the turbulent kinetic energy from two-dimensional data is that the out-of-plane fluctuations $\overline{w'^2}$ are equal to the cross-stream fluctuations $\overline{u'^2}$. With this assumption (and caveat), figure 14 shows the distribution of turbulent kinetic energy within the flow field. Note that the vertical turbulent normal stress $\overline{v'^2}$ is an order of magnitude larger than the horizontal turbulent normal stress $\overline{u'^2}$, so that moderate differences between $\overline{w'^2}$ and $\overline{u'^2}$ will not significantly bias the estimate of k. For the same reason, the estimated contours of k resemble the $\overline{v'^2}$ contours.

Figures 15 and 16 show the horizontal and vertical Favre-averaged turbulent fluxes and scalar variance that can be used for closure of the species equations.

Figure 15(*a*) shows that the peak horizontal turbulent fluxes occur in regions of high horizontal velocity gradient and high plume fluid mass fraction gradients near the plume base, and higher in the plume where the horizontal velocity fluctuations are larger. Figure 15(*b*) shows that the peak vertical turbulent flux is on the centreline, just below the axial position of maximum vertical velocity fluctuations, but within the envelope of the time-averaged plume as defined by mass fraction (figure 8). Figure 16 shows peak scalar variance low in the plume, in the bottom $0.1D$ above the surface of the plume source.

9. Discussion

This work is motivated by the need to understand plume characteristics in turbulent strongly buoyant flows, for which experimental data have been lacking. The ratio of buoyancy to momentum is strongest in the near-source region where the density differences (gradients) are the greatest, and the plume momentum is lowest. The Rayleigh–Taylor instability due to density differences at the base of the plume leads to the vortex that grows to dominate the flow. This process repeats in a cyclical manner.

Virtually all numerical-simulation tools of buoyant flows use Favre-averaged variables to avoid having additional terms that arise from the use of simple time (Reynolds) averaging in variable density fields. The current experiments which simultaneously measure velocity and density fields permit the calculation of Favre variables in the case of a simple mixture of helium and air. However, for more complex flows, such as fires, it is sometimes very difficult to obtain spatially and temporally resolved density fields, and thus to obtain Favre velocity statistics. Figures 9 to 14 include turbulence data calculated as Reynolds (time) averages and as Favre (density-weighted) averages. The Reynolds- and Favre-averaged velocities and turbulent statistics data are the same (to within the uncertainty of the data) and therefore merit further discussion here. If this result is valid for more general buoyant flows, such as fires, then more confidence can be placed on comparison with Reynolds-averaged variables. The Favre-averaged mean velocity statistics are given by (2). Note that mean quantities are functions of position, and fluctuating quantities are functions of position and time. In the simple analysis that follows, the functionality notation will be dropped for simplicity and clarity.

Analyses of their temporal histories throughout the flow field indicate that the vertical velocity and density data appear strongly, but not perfectly, anti-correlated. Example correlation plots are shown in figures 17 and 18, which indicate that the vertical velocity peaks as the density reaches a minimum throughout the flow field. This result is not surprising, as higher acceleration may be expected in a lower-density fluid for a fixed differential pressure field. Analysis of the temporal histories also indicates that the horizontal and vertical velocity peaks are approximately 90° out of phase in regions where both have a significant ($>0.1\,\mathrm{m\,s^{-1}}$) mean velocity. An example is shown in figure 19. This result is not altogether surprising either, since a series of vortical structures passing a measurement point may be expected to produce horizontal minima at vertical maxima, and vice versa, owing to the rolling motion of the structure. It is clear from figure 19 that the energy-bearing structures are largely coherent.

The relationship between the Favre and Reynolds statistics for this type of flow can be illustrated by a simple substitution of approximate functions that represent the observed periodic behaviour and the proper phases of the velocity and density field into the Favre- and Reynolds-averaged definitions of a flow variable.

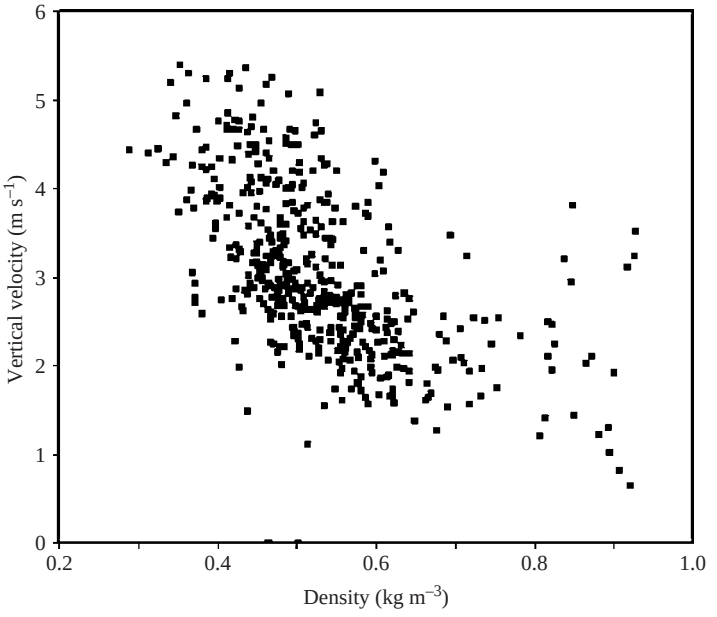

FIGURE 17. Instantaneous vertical velocity *vs.* instantaneous density near the plume centre at the location $x = 0.03$ m, $y = 0.46$ m in Test 29. Similar negative correlation is seen throughout the plume.

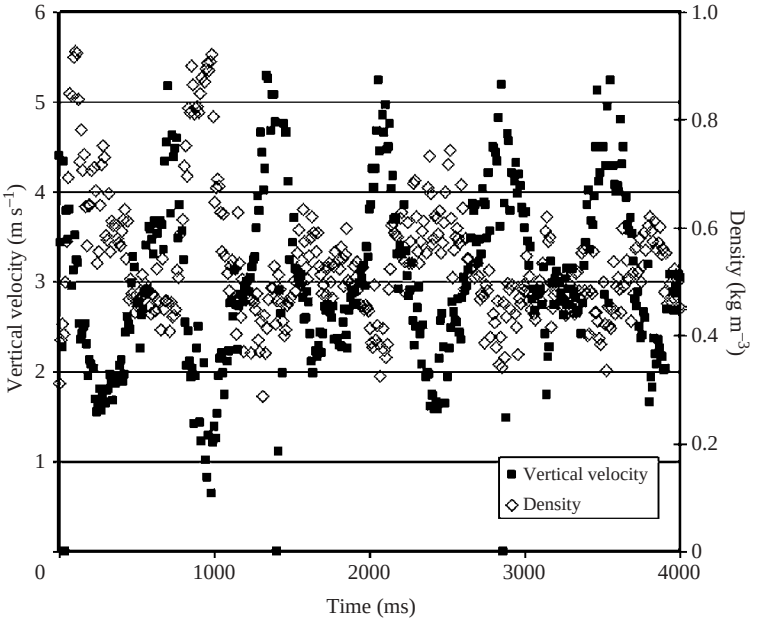

FIGURE 18. Time series of vertical velocity *vs.* density near the plume centre at the location $x = 0.03$ m, $y = 0.46$ m in Test 29. Similar negative correlation is seen throughout the plume.

The phasing of the peaks can be captured with simple sinusoidal functions. Let

$$\rho = \bar{\rho} + \rho^* \sin(\omega t),$$
$$v = \bar{v} - v^* \sin(\omega t),$$
$$u = \bar{u} - u^* \cos(\omega t),$$

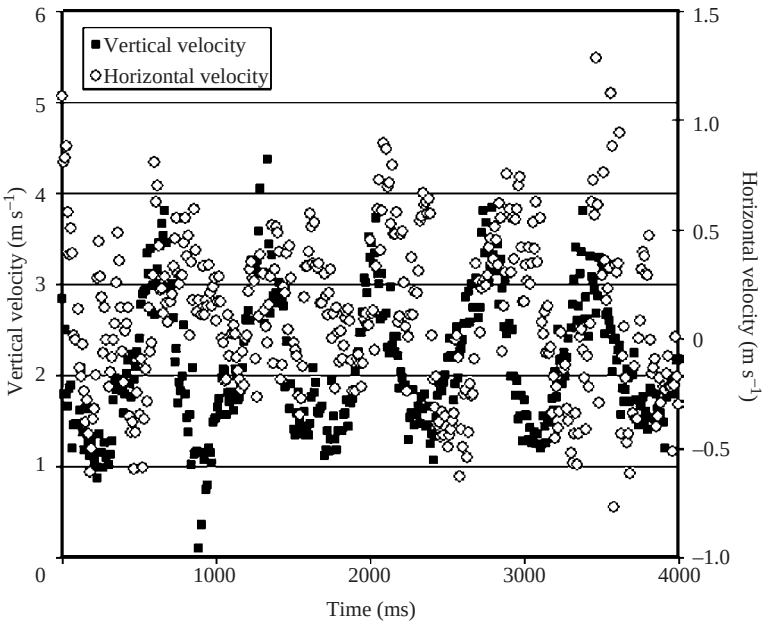

FIGURE 19. Instantaneous vertical velocity *vs.* instantaneous horizontal velocity at the location $x = 0\,\mathrm{m}$, $y = 0.25\,\mathrm{m}$ in Test 29. Similar correlation, approximately 90° out of phase, is seen throughout the plume. Each single-point realization has similar scatter, but the trend is clear.

for the density, and vertical and horizontal components of velocity, respectively. While a sine function is used for example, any periodic function should result in qualitatively the same result.

Substituting for the vertical velocity into (2) gives

$$\tilde{v} = \frac{\int_0^\tau (\bar{\rho} + \rho^* \sin(\omega t))(\bar{v} - v^* \sin(\omega t))\,\mathrm{d}t}{\bar{\rho}\tau}$$
$$= \frac{\int_0^\tau \left[\bar{\rho}\,\bar{v} + \rho^* \bar{v} \sin(\omega t) - \bar{\rho} v^* \sin(\omega t) - \rho^* v^* \sin^2(\omega t)\right]\mathrm{d}t}{\bar{\rho}\tau}. \tag{3}$$

For the vertical velocity, the time integral of the sine function over n cycles is zero, the first-order fluctuation terms are zero, and only the Reynolds average and second-order terms are non-zero.

$$\tilde{v} = \bar{v} - \frac{\rho^*}{\bar{\rho}} \frac{v^*}{2} \tag{4}$$

or

$$\frac{\tilde{v}}{\bar{v}} = 1 - \tfrac{1}{2} \frac{\rho^*}{\bar{\rho}} \frac{v^*}{\bar{v}}. \tag{5}$$

Even for large fluctuations, as in the case of the data here, the difference between Favre- and Reynolds-averaged values is relatively small. For example, (5) shows that for fluctuations of 50 % of the mean in both quantities the difference between Favre and Reynolds is only 12.5 % – within the uncertainty of the data.

A similar argument holds for the horizontal velocity.

$$\tilde{u} = \frac{\int_0^\tau (\bar{\rho} + \rho^* \sin(\omega t))(\bar{u} - u^* \cos(\omega t))\,\mathrm{d}t}{\bar{\rho}\tau} = \frac{\int_0^\tau \left[\bar{\rho}\,\bar{u} + \rho^* \bar{u} \sin(\omega t) - \bar{\rho} u^* \cos(\omega t) - \rho^* u^* \sin(\omega t)\cos(\omega t)\right]\mathrm{d}t}{\bar{\rho}\tau}. \tag{6}$$

Integrating over a fixed number of cycles of sin, cos or sin*cos functions will result in a zero mean. In this case, the Favre and Reynolds statistics are remarkably identical.

$$\tilde{u} = \bar{u}. \tag{7}$$

The Reynolds-averaged fluctuations are given as

$$u_i' = u_i(t, x_k) - \bar{u}_i, \tag{8}$$

and the Reynolds-averaged Reynolds stresses are given as

$$\overline{u_i' u_j'} = \frac{1}{\tau}\int_0^\tau (u_i(t, x_k) - \bar{u}_i)\left(u_j(t, x_k) - \bar{u}_j\right)\mathrm{d}t. \tag{9}$$

Substituting for the normal vertical stress, as an example, gives

$$\overline{v'v'} = \frac{1}{\tau}\int_0^\tau (v^* \sin(\omega t))(v^* \sin(\omega t))\,\mathrm{d}t = \tfrac{1}{2} v^* v^*, \tag{10}$$

and similarly for the normal horizontal stress. Note that in this perfectly correlated example, the Reynolds stress, $\overline{u'v'}$, would be zero. The Reynolds stress is not zero in the data, but, consistent with this analysis, it is about an order of magnitude less than the normal vertical stress.

The Favre-averaged turbulent velocity fluctuations are given by

$$u_i'' = u_i(t, x_k) - \tilde{u}_i, \tag{11}$$

and the Favre-averaged Reynolds stresses are given as

$$\frac{\overline{\rho u_i'' u_j''}}{\bar{\rho}} = \frac{1}{\bar{\rho}\tau}\int_0^\tau \rho(t, x_i)(u_i(t, x_k) - \tilde{u}_i)(u_j(t, x_k) - \tilde{u}_j)\,\mathrm{d}t. \tag{12}$$

Note that

$$u_i(t, x_i) - \tilde{u}_i = u_i(t, x_k) - \bar{u}_i + (\bar{u}_i - \tilde{u}_i), \tag{13}$$

and

$$\left.\begin{aligned} \bar{u}_i - \tilde{u}_i &= 0, \\ \bar{v}_i - \tilde{v}_i &= \frac{\rho^* v^*}{2\bar{\rho}} \equiv \delta v. \end{aligned}\right\} \tag{14}$$

Substituting into the integral for the vertical normal stress gives,

$$\begin{aligned} \frac{\overline{\rho v'' v''}}{\bar{\rho}} &= \frac{1}{\bar{\rho}\tau}\int_0^\tau (\bar{\rho} + \rho^* \sin(\omega t))\left(\delta\bar{v} - v^* \sin(\omega t)\right)\left(\delta\bar{v} - v^* \sin(\omega t)\right)\mathrm{d}t. \\ &= \frac{1}{\bar{\rho}\tau}\int_0^\tau [(\bar{\rho} v^* v^* - 2 v^* \rho^* \delta\bar{v}) \sin^2(\omega t) + \bar{\rho}\delta\bar{v}^2 \\ &\quad + (\delta\bar{v}^2 \rho^* - 2 v^* \bar{\rho}\delta\bar{v}) \sin(\omega t) + \rho^* v^* v^* \sin^3(\omega t))]\,\mathrm{d}t. \end{aligned} \tag{15}$$

Integrating over n cycles, the odd power sine terms are zero. Integrating and substituting gives:

$$\frac{\overline{\rho v'' v''}}{\bar{\rho}} = \tfrac{1}{2} v^* v^* - \rho^* v^* \delta\bar{v} + \delta\bar{v}^2 = \tfrac{1}{2} v^* v^* \left(1 - \tfrac{1}{2}\left(\frac{\rho^*}{\bar{\rho}}\right)^2\right) = \overline{v'v'}\left(1 - \tfrac{1}{2}\left(\frac{\rho^*}{\bar{\rho}}\right)^2\right). \quad (16)$$

Since the Reynolds and Favre means are identical in this simple perfectly correlated example, substitution for the horizontal normal stress gives:

$$\begin{aligned}\frac{\overline{\rho u'' u''}}{\bar{\rho}} &= \frac{1}{\bar{\rho}\tau}\int_0^\tau (\bar{\rho} + \rho^* \sin(\omega t))(u^* \cos(\omega t))(u^* \cos(\omega t))\,\mathrm{d}t \\ &= \frac{1}{\bar{\rho}\tau}\int_0^\tau \left[\bar{\rho} u^* u^* \cos^2(\omega t) + \rho^* u^* u^* \cos^2(\omega t)\sin(\omega t))\right]\mathrm{d}t. \end{aligned} \quad (17)$$

Integrating over n cycles, the second term is zero so that the Reynolds and Favre horizontal stresses are identical. In this perfectly correlated example, the Favre and Reynolds statistics are the same to lead order. While the data are not as perfectly correlated as suggested by this simple analysis, the data are reasonably correlated, and the Favre- and Reynolds-averaged statistics do match to lead order.

This result suggests that even though there is a turbulent cascade present in the current data, the largest structures are still relatively coherent (i.e. as established by the reasonably constant puffing frequency) and thus the velocity and concentration fields have established phase relations. These large coherent structures dominate the fluctuating intensities so the Favre and Reynolds statistics are the same to lead order. The flow chosen for this study, the near-source region of a turbulent buoyant plume where the flow momentum is minimized and the density difference (sharpness of the density gradients) is maximized, is the limiting case of a buoyancy-dominated flow. The other extreme turbulent flow limit is the momentum-dominated limit where the flow momentum is maximized and the density differences are minimized. At each limit, the difference between Favre- and Reynolds-averaged statistics is at most second order, in the buoyant limit because of strong correlation with cancelling phase relationships and in the momentum limit because of vanishing density fluctuations. In between these limiting cases, the differences will depend on the degree of correlation between the density and velocity fluctuations, which may or may not be in phase. A careful study (either experimental or computational) on a mixed buoyancy/momentum flow may produce estimates of physical bounds on the expected differences between Favre- and Reynolds-averaged statistics.

10. Summary and conclusions

Simultaneous PIV and acetone PLIF have been performed on a 1 m base diameter buoyant helium plume. The data cover 70 puff cycles of the plume. Instantaneous two-dimensional velocity plots are obtained for each time plane (146 time planes per puff cycle, on average) spaced 5 ms apart. Each vector represents a statistical estimate of the velocity in a 2.1 cm × 2.1 cm × 0.8 cm volume, with volumes overlapped by 50 % in the vector plots. Time-averaged turbulent statistics ($\overline{u'^2}$, $\overline{v'^2}$, $\overline{u'v'}$, an estimate of k, and turbulent fluxes) are also presented. The joint velocity and mass fraction data are used to calculate Favre-averaged statistics within the plume. The results clearly show the dominant effect of puffing, measured at 1.37 cycles s^{-1} for this plume, on the temporal and spatial development of the velocity field. The large puffing vortex is shown to be initiated by a classical Rayleigh–Taylor instability at the base of the

plume. The data are useful in developing an understanding of, and validation of, computational models to predict the behaviour of buoyant turbulent plumes.

Little difference is seen between the Reynolds- and Favre-averaged statistics. A simple analysis was performed to determine the expected differences in such flows and the results show that in a flow with perfectly correlated velocity and density fields with phase relationships as suggested by the data, the Favre and Reynolds statistics are the same to lead order. Thus, in the limit of buoyancy-dominated flows, the coherent phase relationships between the density and velocity fields minimize the difference between Favre and Reynolds first- and second-order statistics.

A large team contributed to this multiyear effort. Special thanks for – Scientific cinematography: Amarante Martinez, Mark Nissen and Leroy Perea; Experimental operations: Tom Blanchat, Rod Oliver, Chuck Hanks, Tom Grasser, Phil Reyes, Bennie Belone and Michael Ramirez; Image processing assistance: Chad Young, Kevin Thomson and Wendy Corriveau Taylor; Data analysis assistance: Ryan Davies, Jeremy Fortier and Monica Hands. Ken Christensen of the University of Illinois was very helpful in optimizing the performance of PIV Sleuth and in developing the Matlab vorticity algorithms. Thanks to Snezhana Abarzhi for first pointing out the Rayleigh–Taylor bubble and spike structures to the authors, who invariably were focused on the large-scale puffing. Comparison of time- and spatially-resolved numerical simulations with time- and spatially-resolved experimental data is very insightful and the authors of this experimental paper are indebted to the insights gleaned from their numerical colleagues, Paul DesJardin, Heinz Pitsch and Guillaume Blanquart. The authors appreciate the support of program managers for the DOE/Sandia LDRD, ESRF and Campaign 6 programs. Sandia is a multiprogram laboratory operated by Sandia Corporation, a Lockheed Martin Company, for the United States Department of Energy under Contract DE-AC04-94AL85000.

REFERENCES

Blanchat, T. K. 2001 Characterization of the air source and plume source at FLAME. Sandia National Laboratories, SAND2001-2227.

Blinov, V. I. & Khudyakov, G. N. 1961 Diffusion burning of liquids. (English Trans.) US Army Engineering Research and Development Laboratories, Fort Belvoir, VA, Rep. AERDL-T-1490-a-c. ASTIA, AD 296762.

Cetegen, B. M. 1997 Measurements of instantaneous velocity field of a non-reacting pulsating buoyant plume by particle image velocimetry. *Combust. Sci. Tech.* **123**, 377–387.

Cetegen, B. M. & Ahmed, T. A. 1993 Experiments on the periodic instability of buoyant plumes and pool fires. *Combust. and Flame* **93**, 157–184.

Cetegen, B. M. & Kasper, K. D. 1996 Experiments on the oscillatory behaviour of buoyant plumes of helium and helium-air mixtures. *Phys. Fluids* **8**, 2974–2984.

Christensen, K. T., Soloff, S. M. & Adrian, R. J. 2000 PIV Sleuth – integrated particle image velocimetry interrogation/validation software. *TAM Rep.* **943**, University of Illinois.

Dai, Z. & Faeth, G. M. 1996 Measurements of the structure of self-preserving round buoyant turbulent plumes. *J. Heat Transfer* **118**, 493–495.

DesJardin, P. E., Tieszen, S. R., O'Hern, T. J. & Gerhart, A. L. 2000 Numerical predictions and experimental measurements of the near-field of a large turbulent helium plume. *ASME Intl Mech. Engng Conf. and Exposition, Symp. on Integrated Experimental and Simulation Investigations in Research and Design, Orlando, FL, November.*

DesJardin, P. E., O'Hern, T. J. & Tieszen, S. R. 2004 Large eddy simulation and experimental measurements of the near-field of a large turbulent helium plume. *Phys. Fluids* **16**, 1866–1883.

Keane, R. D. & Adrian, R. J. 1992 Theory of cross-correlation analysis of PIV images. *Appl. Sci. Res.* **49**, 191–215.

Lozano, A., Yip, B. & Hanson, R. K. 1992 Acetone: a tracer for concentration measurements in gaseous flows by planar laser-induced fluorescence. *Exp. Fluids* **13**, 369–376.

Megerle, M., Sick, V. & Reuss, D. L. 2002 Measurement of digital particle image velocimetry precision using electro-optically created particle-image displacements. *Meas. Sci. Tech.* **13**, 997–1005.

Papanicolaou, P. N. & List, E. J. 1988 Investigations of round vertical turbulent buoyant jets. *J. Fluid Mech.* **195**, 341–391.

Pasamarthi, K. S. & Agrawal, A. K. 2003 Schlieren measurements and analysis of concentration field in self-excited helium jets. *Phys. Fluids* **15**, 3683–3692.

Shabbir, A. & George, W. K. 1994 Experiments on a round turbulent buoyant plume. *J. Fluid Mech* **275**, 1–32.

Soteriou, M. S., Dong, Y. & Cetegen, B. M. 2002 Lagrangian simulations of the unsteady near field dynamics of planar buoyant plumes. *Phys. Fluids* **14**, 3118–3140.

Thurber, M. C., Grisch, F. & Hanson, R. K. 1997 Temperature imaging with single- and dual-wavelength acetone planar laser-induced fluorescence. *Optics Lett*. **22**, 251–253.

Tieszen, S. R., O'Hern, T. J., Weckman, E. J. & Schefer, R. W. 2004*a* Experimental study of the effect of fuel mass flux on a one meter diameter methane fire and comparison with a hydrogen fire. *Combust. and Flame* **139**, 126–141.

Tieszen, S. R., O'Hern, T. J., Schefer, R. W., Weckman, E. J. & Blanchat, T. K. 2002 Experimental study of the flow field in and around a one meter diameter methane fire. *Combust. Flame* **129**, 378–391.

Tieszen, S. R., O'Hern, T. J., Schefer, R. W. & Perea, L. D. 1998 Spatial and temporal resolution of fluid flows: LDRD final report. Sandia National Laboratories, SAND98-0338.

Tieszen, S. R., Pitsch, H., Blanquart, G. & Abarzhi, S. 2004*b* Toward the development of a LES-SGS closure model for buoyant plumes. *Proc. Summer Program 2004, Center for Turbulence Research, Stanford, University, Stanford CA*, pp. 341–352.

Willert, C. 1996 The fully digital evaluation of photographic PIV recordings. *Appl. Sci. Res.* **56**, 79–102.